www.DeepakPublishing.com

Desselle, R. et al. (2017): JoSS, Vol. 6, No. 3, pp. 635–650
(Peer-reviewed article available at www.jossonline.com)

www. JoSSonline.com

A 3U CubeSat to Collect UV Photometry of Bright Massive Stars

Richard Desselle, Christian Kintziger, and Pierre Rochus

Centre Spatial de Liège, University of Liège
Liège, Belgium

Gregor Rauw and Yaël Nazé

Groupe d'Astrophysique des Hautes Energies
University of Liège
Liège, Belgium

Abstract

The last decade has witnessed exciting progress with the miniaturization of essential components of spacecraft, leading to the development of nano-and micro-satellites beyond their use as mere technological experiments. These small satellites are now considered to be important complements of much larger and more sophisticated probes to conduct scientific research. In this context, the current authors have conducted a feasibility study of a near-ultraviolet (UV) telescope onboard a three-unit (3U) CubeSat. The scientific purpose of this payload will be to collect time series of photometric measurements of bright, mainly massive, stars down to an optical magnitude of V=5. This paper presents the optimized optical design of the payload and its associated detector. It further discusses the system accommodation and integration, as well as a providing a preliminary mission analysis. A photometric budget taking into account the characteristics of the target stars and the payload performances is also presented. This feasibility study demonstrates that it is possible to conduct a robust science mission using a very small satellite at limited cost.

1. Introduction

1.1. Astrophysical Background

Since the termination of the International Ultraviolet Explorer (IUE) mission in 1996 and the end of the Far Ultraviolet Spectroscopic Explorer (FUSE) in 2007, the ultraviolet (UV) domain suffers from a lack of dedicated instrumentation. Indeed, the situation is very different from other wavelength domains. The optical and near-IR (infrared) wavelength ranges can be observed from the ground at many observatories. Moreover, several far-IR space observatories are under construction or in planning. However, there is currently no mid-to far-UV mission at a similar level of preparation, though the UV domain has great diagnostic potential, especially for the study of bright massive stars whose spectral energy distribution peaks in the UV. Spectroscopy clearly offers the highest scientific return, as many chemical elements have strong resonance lines in this wavelength domain. The analysis of such lines provides sensitive diagnostics of the stellar and wind parameters. However, high-resolution

Corresponding Author: Richard Desselle, rdesselle@ulg.ac.be
Publication History: Submitted – 03/21/17; Revision Accepted – 11/08/17; Published – 01/30/18

spectroscopic astronomical missions require large aperture telescopes. This can only be accommodated on medium or large space missions (e.g. Gómez de Castro et al., 2014). On the other hand, as demonstrated by the Optical Monitor (OM) instrument on-board XMM-Newton (Mason et al., 2001), sensitive UV photometry can be performed with much smaller telescopes. In particular, monitoring the photometric variations of stars has an important scientific return. Such data are of paramount importance for asteroseismology, where measuring the radial and non-radial pulsations of stars allows probing the physical conditions in their interiors (e.g. Handler, 2013). In asteroseismology, an important problem, especially for massive stars, is the identification of pulsation modes. Such an exercise requires multicolor photometric time series. The UV data are especially important here to complement optical data because the relative amplitudes of the photometric changes are larger at shorter wavelengths (Aerts et al., 2010). Space-borne platforms constitute an essential tool in this context, as they overcome the limitations due to variable atmospheric absorption as well as the long daily gaps measurements. However, the power of such data is not restricted to asteroseismology. Illustrations are the intriguing CoRoT light curves of early-type stars in NGC 2244 (Blomme et al., 2012, and references therein), or the detection of flaring activity and rotational modulation in magnetically active late-type stars with Kepler (Davenport, 2016). In addition, accurate space-borne UV photometry also allows studying the development of disks around Be stars, as well as many phenomena linked to binary interactions (i.e., tidal deformations, eclipses, etc.).

1.2. Proposed Instrument and Mission

Ambitious, sophisticated space observatories are complex and expensive (typically around 1 billion euros), usually restricting their construction and operation to major space agencies. FUSE, for example, was a NASA mission whose development was led by the Johns Hopkins University. Collaborators originated from other universities (Boulder and Berkeley) and international partners, such as the Canadian and the French Space Agencies (Conard et al., 2000). In the same vein, the IUE mission was an international collaboration between NASA, the European Space Agency and the United Kingdom's Science and Engineering Research Council (Bogges et al., 1978).

The situation is different for CubeSats, which are built from one or several $10 \times 10 \times 10$ cm^3 units. Over recent years, it has been demonstrated that such CubeSats can be developed by small teams and successfully used for scientific research for a typical cost of a few million euros (Woellert et al., 2011). In the same field of application as the current project, the BRITE constellation (Weiss et al., 2014) and the ExoplanetSat (now called ASTERIA) project (Smith et al., 2010) provide good illustrations of CubeSats being used or developed for the study of stars and their environment. CubeSats cannot compete with large, expensive space observatories, but they can complement them, and fill some niches that are not covered by the larger facilities.

In this context, the current paper presents a feasibility study of a new space-borne near-UV telescope that could be installed onboard a three-unit (3U) CubeSat. The aim of the telescope is to acquire photometric time series of bright, mainly massive, stars between 2500 and 3500 Å. Such a mission has never been performed before. Indeed, most scientific CubeSats are designed for Earth and atmosphere observations, cosmic rays detection, or stellar observations in the visible domain (Swartwout, 2013). Observing in the UV prevents the use of a refractive telescope composed of lenses such as used for BRITE. These configurations are generally more compact, and thus more suitable for such small platforms. This study's goal is to reach the scientific requirements summarized in Table 1. These

Table 1. Scientific Requirements for the Proposed Near-UV Telescope

Parameter	Requirement	Goal
Spectral range	2500–3500 Å	N/A
Angular resolution	15 arcsec	10 arcsec
Field of view (diameter)	1°	2°
Target magnitudes	$V \leq 4$	$V \leq 5$
Photometric accuracy	0.001 mag	0.0005 mag
Typical exposure time	5 min	1 min
Mission duration	2 years	4 years
Duty cycle	60%	75%

requirements are inspired by the OM instrument onboard XMM-Newton (Mason et al., 2001), but scaled for a smaller telescope size. They also take into account security margins which anticipate the limitations of very small platforms. The current study aims to use the smallest possible spacecraft platform, which is the 3U CubeSat. Indeed, a smaller platform would not allow designing a telescope sufficiently sensitive to meet the specifications while carrying the elements necessary for the operation of the satellite. In view of numerous successful 3U CubeSat scientific missions, such as CINEMA or EXOCUBE (NSF-NASA, 2013), one can be confident that a 1.5U volume is sufficient to accommodate the service module. Nevertheless, achieving the photometric accuracy with a small telescope is a great challenge. Section 2 discusses the optical design, Sections 3 and 4 present the components and orbit to be used, and Section 5 examines the photometric budget. Concluding remarks are found in Section 6.

2. Optical Design

2.1. Basic Considerations and Constraints

Since the transmission of lenses is very poor in the UV, reflecting optics must be used. The baseline design in the current study is thus a Ritchey-Chrétien telescope composed of two reflective hyperbolic mirrors. This kind of telescope has advantages such as a high optical performance with only two reflective surfaces, as well as a large aperture. Preliminary research on off-the-shelf components for CubeSat revealed that at least 1.5U is needed for vital sub-units such as electronics, communication, attitude controller, etc. The payload is thus constrained to fit into the remaining 1.5 CubeSat units, with the optical axis oriented along the CubeSat length to benefit from the largest focal length possible. The mirrors are coated with a specific UV aluminum coating (Melles Griot, 2016), offering an average reflectance of 87% over the spectral domain of the instrument. To reject unwanted light that could reach the telescope's focal plane, two devices will be implemented. First, a UV filter (Schott, 2016) will be placed directly in front of the focal plane to reject the light of wavelengths outside the [2500, 3500] Å range (surface #4 in Figure 1). In addition, a baffling system will be installed on the two mirrors to reject the light from outside of the scientific field of view (FoV).

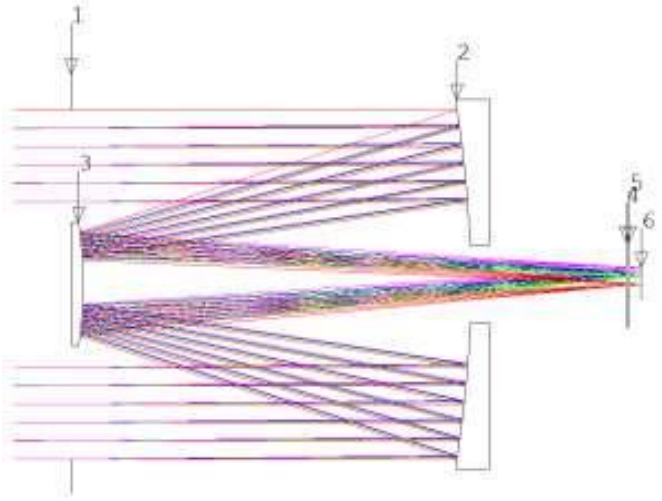

Figure 1. A 2D view of the near-UV telescope optical design and the representation of several off-axis rays passing through the entrance pupil and reaching the focal plane. Surfaces: #1 = entrance pupil of the telescope, #2 = primary mirror, #3 = secondary mirror, #4 = front face of the UV-filter, #5 = back side of the UV-filter and #6 = focal plane.

2.2. Design Characteristics

2.2.1. Optimization Workflow

The optimization process consists in obtaining an optical design that fulfills both the scientific requirements and the inherent constraints of a CubeSat payload. A first constraint is the diameter of the entrance aperture of the telescope (surface #1 in Figure 1). This latter is set to 90 mm to maximize the amount of light collected by the telescope while simultaneously respecting the volume constraints given by an off-the-shelf 3U CubeSat structure (ISIS Space, 2017). Then, the allocated room for the optical design is fixed to 1.5U for the reasons previously explained.

Typical near-UV optimized detectors exhibit pixel sizes of 13 or 26 µm (e.g. Teledyne e2v, 2017). It was decided to use 13 µm pixels as a baseline, to reduce the dimensions of the entire focal plane. The smaller pixel dimension also enables the use of shorter focal lengths for a given angular resolution and eases the coupling of the optical design to its CubeSat architecture.

Anticipating saturation issues (addressed in Section 5.3), the study fixed the number of pixels illuminated by the PSF at four. Therefore, the light of an observed star will spread onto a square of 26 µm side to relax the photometric budget of the instrument. Knowing the pixel size and the required angular resolution of 15 arcsec (Table 1), the minimum required effective focal length f_{eff} is evaluated to 357.5 mm.

The above constraints and requirements were then set in Code V to obtain an optimized telescope that fits within 1.5 units of a CubeSat. Another critical parameter is the obstruction by the secondary mirror (surface #3 in Figure 1). The goal during the design process was thus to minimize the size of this element to maximize the incoming photon flux. For that purpose, several mechanical layouts of the telescope within the range of the strict CubeSat volume constraints were studies, and the one that fit the above considerations was selected.

The final value of f_{eff} after optimization amounts to 487.5 mm, yielding an angular resolution of 11 arcsec. The study was therefore able to take advantage of the available platform room and surpass the requirement in Table 1. It also achieved a reduction in light transmission due to the obstruction of only 13% (without the baffling system presented in Section 2.2.3), which is completely acceptable for the current application, as will be demonstrated with the photometric budget described in Section 5. The 2D layout of the telescope and the associated characteristics are presented in Figure 1 and Table 2, respectively.

Table 2. Geometrical Characteristics of the Near-UV Telescope Presented in Figure 1

Parameter	Requirement
Entrance aperture diameter (surface #1)	90 mm
Primary mirror diameter (surface #2)	92 mm
Secondary mirror diameter (surface #3)	32 mm
Effective focal plane diameter (surface #6)	12 mm
Distance between surface #1 and surface #2	100 mm
Distance between surface #1 and surface #4	143 mm
Distance between surface #1 and surface #6	147 mm

Attempts to increase the size of the FoV beyond the required diameter of 1° revealed a very fast degradation of the PSF for large off-axis angles. This degradation of the PSF was due to astigmatism, the main aberration suffered by the Ritchey-Chrétien telescopes (Figure 2). Optimizing the telescope efficiency up to

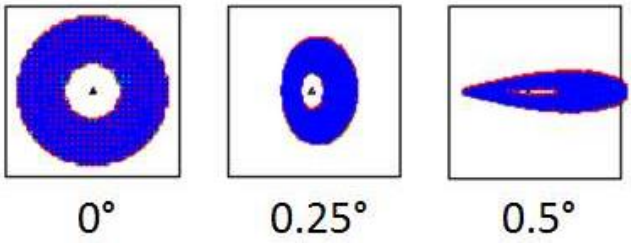

Figure 2. Spot diagrams of the designed photometer for squared areas of 26 µm side considering 3 off-axis angles (0, 0.25 and 0.5° from left to right).

2° led to the use of complex optical surfaces and large central obstructions. It was decided to favor simplicity and the light transmission of the selected design for our CubeSat baseline. On the other hand, photometric measurements may still be carried out slightly beyond 1° with the somewhat degraded angular resolution.

2.2.2. Spot diagrams

The spot diagrams for several off-axis positions are shown in Figure 2 where the squares are 26 × 26 µm since the system is optimized to fit the spot onto four pixels of 13 µm size. As can be seen for small off-axis angles (0° and 0.25°), the light is uniformly (or quasi-uniformly) spread over the bundle of pixels illuminated at the focal plane. For larger angles (near 0.5°), the spot is elongated along the radial direction. The flattening of the spot is typical of astigmatism optical aberration. This degradation of the PSF uniformity has implications on the data reduction, although observations of fields with several bright stars ($V \leq 5$) falling into the FoV of the instrument will be the exception rather than the rule. Thus, the degradation of the spot uniformity for large off-axis angles is not considered to be an issue. It was also noted that the central holes that appear in all the spots are simply due to the central obscuration at the entrance pupil of the telescope.

2.2.3. Baffling System and Stray Light Analysis

As all telescopes do, Ritchey-Chrétien telescopes suffer from stray light when not protected by an optical

baffle. A baffling system was designed in this study, based on procedures described by Terebizh (2001) to prevent stray light from directions outside the FoV from reaching the focal plane. This enables a geometrical optimization of the baffles to block unwanted light from the sky while simultaneously minimizing the obscuration of the system by the baffle placed on the secondary mirror M2. This concept is based on two conic baffles located in front of the two mirrors. A main baffle surrounding the overall instrument and some vanes on each baffle were also added, to block internally-reflected, second-order stray light. The final configuration of the baffling system installed on the telescope is presented in Figure 3. Considering this final layout, the study was able to reassess the value of the effective diameter of the telescope. The secondary mirror and its baffle produce an obscuration equivalent to a diameter of 38 mm that must be compared to the 90 mm diameter of the entrance pupil, leading to a telescope effective diameter equal to 81.5 mm, and corresponding to a reduction in light transmission of 17% compared to the 13% without the baffling system. The new effective diameter will be used in our photometric budget computation in Section 5.

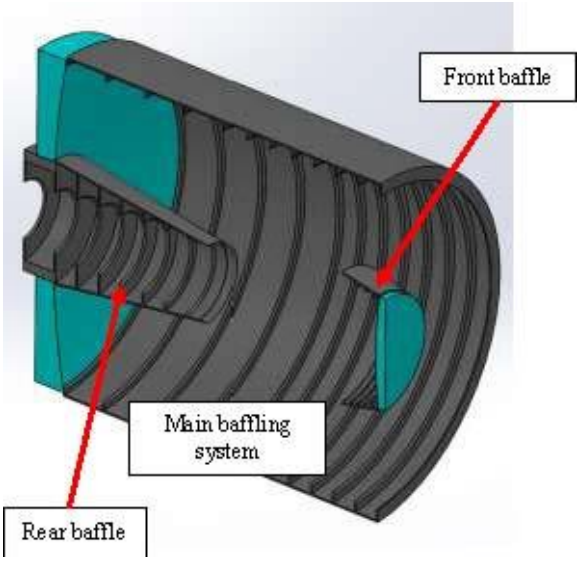

Figure 3. Cross-sectional view of the baffling system integrated around the optical design.

Using the ASAP software, this study quantified the relative amount of photons coming from off-axis angles of an entire sky hemisphere, entering the telescope, and reaching the focal plane. This quantity was determined by defining a light source covering a part or the entire focal plane, and then assuming that this source emits light in one hemisphere in the direction of the secondary mirror. The light is then back-propagated through the telescope until it reaches the entrance pupil. Those photons are then sorted according to their incidence angle on the pupil to identify the off-axis fields reaching the detector since their propagation path is reversible. This method is commonly used, since any simulation using the direct path cannot simulate an infinite set of FoVs. For modeling, the inner walls of the baffles are coated with Chemglaze (black coating with very low reflectance) (Persky, 1999), but they still induce some scattered reflections. The study also used the Harvey model (Harvey, 1975) for characterizing the reflections on the mirrors, more specifically their scattering behavior with respect to roughness.

Figure 4 presents the relative quantity of photons that pass through the telescope and reach the central position on the focal plane as a function of their off-axis angles (measured from the center of the FoV (0°,0°)). From this figure, it can be seen that the maximum is naturally reached on-axis at (0°,0°). However, scattered light enables some other fields of view to reach these pixels too. Nevertheless, the levels of those directions are below 0.0001% of the on-axis maximum level. When the entire noise over the hemisphere is integrated, assuming a uniform emission, it was found that for one effective photon from (0°,0°), 0.007 photon is also obtained from the rest of the field.

To assess the effective level of stray light, the brightness of a sky hemisphere must be evaluated as it will be seen from space. According to Roach (1964), there are two main contributions: stellar and zodiacal light. Using the results of Leinert et al. (1998) and Gonhalekar et al. (1980), it was estimated that the combined amount of light from these contributions at the entrance of our instrument is $N_{SL} = 8.73 * 10^7$ photons/cm².s over the 2500–3500 Å range for an entire hemisphere. This value will be associated to a noise parameter in the photometric budget.

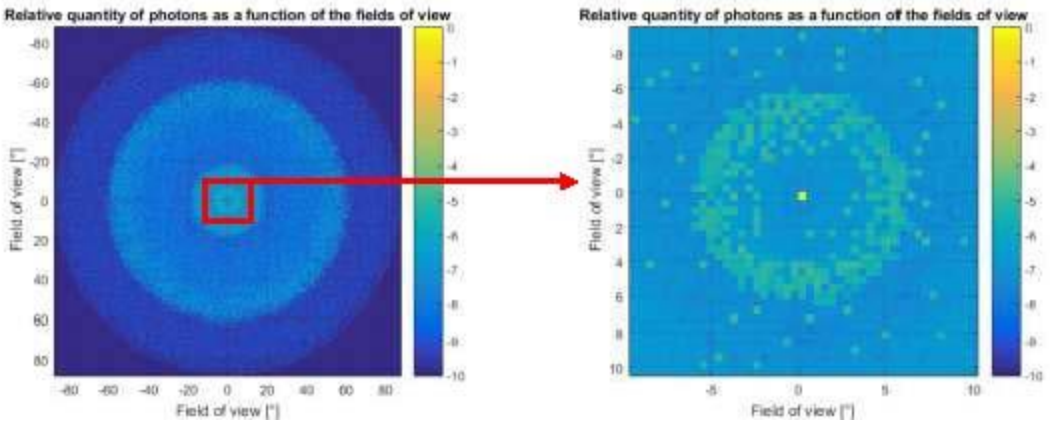

Figure 4. Relative quantity of photons, passing through the instrument and reaching the central position of the focal plane, as a function of the fields of view/off-axis angles over an entire hemisphere of the sky. The quantity of photons is given in a logarithmic scale.

3. System Overview

3.1. Solar Panels Configuration

Figure 5 shows the design of the 3U CubeSat with its solar panels in a table configuration. It can be seen that the payload fits into 1.5U as it was chosen. The other half of the S/C is dedicated to the sub-units needed to obtain a fully operational satellite. The volumes of these units (top and bottom parts of Figure 5) are simulated using computer-aided designs (CAD) of

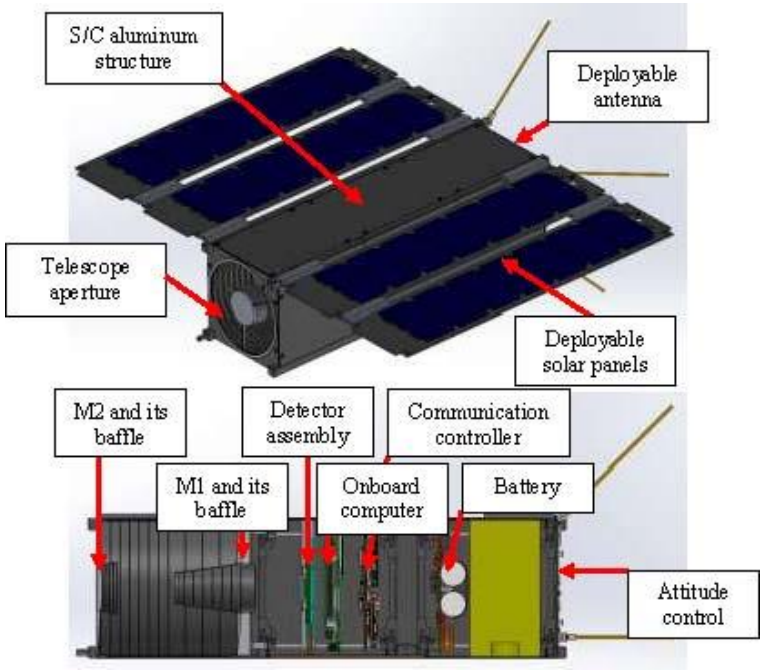

Figure 5. Overview and cross-sectional side-view of the table configuration of the 3U CubeSat. Bottom figure from left to right: the secondary mirror and its baffle which are mounted on a support linked to the S/C structure by three thin feet; the primary mirror and its baffle which are mounted on a support directly fixed to the spacecraft structure; the detector assembly composed of the detector, an electronic card, a thermal insulation made of Permaglas, an aluminum structure and a radiator; the onboard computer (CAD from ISIS Space, 2017); the communication controller (CAD from GOMSpace, 2017); the battery (CAD from GOMSpace, 2017); the attitude determination and control system (ADCS) (volume from Blue Canyon Technologies, 2017); and the deployable antenna (CAD from GOMSpace, 2017).

some components off-the-shelf (COTS) from several manufacturers. The sub-units will be briefly discussed in Section 4.3. Four deployable solar panels are represented.

During the design process, the table configuration was compared to a cross one where the solar panels are attached to the opposite side of the telescope aperture. The comparison was made with respect to the constraints on the sky visibility of the two configurations, assuming the satellites in the same orbit presented in Section 4.1. The cross configuration solution suffered from a lack of pointing flexibility because it is highly constrained by its Sun aspect angle for the power generation and also avoidance zones where the Earth or the Moon could be in the field of view. The table configuration is able to point in almost any direction in the sky for scientific observation during the mission while the sky visibility of the cross configuration is restricted to a narrow band of the sky around the ecliptic, explaining our preference for the table configuration.

3.2. Detector Characteristics

To reach a high efficiency in the near-UV, it is best to use a back-illuminated, thinned CCD detector. As an example, an off-the-shelf detector from e2v (e2v Technologies, 2017) that is suitable for the current application was identified. The main characteristics of the detector are shown in Table 3. The UV-coated CCD has a non-constant quantum efficiency ranging between 55% and 75% in the spectral domain under consideration.

Table 3. Characteristics of the CCD47-20 from e2v (e2v Technologies, 2017)

Parameters	Value
Pixel size	13X13 μm
Number of pixels	1024X1024
Full well capacity (peak)	100 ke^-/pixel
Dark signal at 0°C (at −40°C)	25 e^-/pixel s (0.05 e^-/pixel s)
Charge transfer efficiency	99.9 %
Readout noise at 20 kHz	2 rms e^-/pixel
Maximum readout frequency	5 MHz

3.3. Data storage and transfer

Current printed circuit boards proposed for CubeSat applications are designed with several ports for memory cards up to 8 GB. It is reasonable to assume that onboard data storage capacity will be at least 16 GB. A scientific image size can be quantified using the number of pixels (Table 3). Assuming that each pixel contains 32 bits of information, the size of each image is evaluated at 4.19 MB. If memory cards are only used for storing scientific data, they are able to receive more than 3800 images before saturating.

Table 1 indicates a duty cycle goal of 75%. In other words, it assumes that 75% of the mission is dedicated to scientific observation. Anticipating the orbit definition (Section 4.1), the duty cycle could be translated into approximately 75 min per orbit, considering the period of Table 4. If the observation time goal of 1 min (Table 1) is reached, 75 images will be acquired per orbit, which corresponds to 314.25 MB stored in memory cards. It will then take a little bit more than 50 revolutions to fill up the entire memory.

Table 4. Orbital Parameters of a Dusk-dawn SSO for a Launch on January 1, 2020, at midnight. The Parameters have been Defined Using the J2 Propagator of the Satellite Tool Kit (STK) Software

Parameters	Value
a, semi-major axis	7178.14 km
e, eccentricity	5.70681e-16
i, inclination	98.5880°
Ω, RAAN	190.128°
ω, argument of periapsis	0°
ν_0, true anomaly at launch 0.1089°	0.1089°
T, period	100.8735 min

Off-the-shelf antenna and communication controllers are numerous for CubeSats. From research on manufacturers' websites, a data transfer rate up to 100 kbps is considered for a preliminary data transfer evaluation. In terms of image transfer, it would take 5 minutes and 35 seconds to download a full image from the spacecraft to the ground station – i.e., more than five times longer than the time of data acquisition.

Hence, it is not possible to download full images while respecting the duty cycle requirement. Restricting the data to a window of 100 × 100 pixels will reduce the image size by a factor of approximately 100, which will be easier to handle with a COTS antenna. Such a window of 100 × 100 pixels is sufficient to collect the signal of a target star and also the background for data reduction. Since the mission is designed to observe bright stars, which are relatively isolated, such a windowing will not reduce the scientific return. However, if several targets were to be observed simultaneously, the windowing algorithm associated to the CCD electronics would need to be adapted to enlarge the window or to select several windows corresponding to each star of interest. It could be anticipated by establishing a very precise and complete observation plan for the entire mission.

4. Thermal Environment and Analysis

4.1. Orbit Definition

The strategy for orbit definition was to maximize the duration of sunlight exposition to benefit from a maximal power supply. It was also a goal to minimize the Sun exposure variation over the lifetime of the mission. Considering these constraints, a dusk-dawn Sun-synchronous orbit (SSO) was chosen that provides a relatively constant and maximal solar exposure during the mission. It was also assumed that the orbit would be a low Earth orbit with an altitude not higher than 800 km. A hypothetical launch date of January 1, 2020, at midnight, was used. The associated orbital parameters are presented in Table 4.

The propagation of the orbit of Table 4 with the STK software allows analyzing, for a two-year mission, the percentage of eclipse over a full orbit as a function of time (Figure 6). From Figure 6, it is known that 148 days of the entire mission (±20%) are subject to an eclipse with a maximum duration reaching 17% of the orbit (i.e., 17 min per orbit). Since there are eclipses, even though not all the time, an on-board battery is required. The knowledge of the illumination also provides direct constraints for the thermal design of the spacecraft (see further details in the next Section).

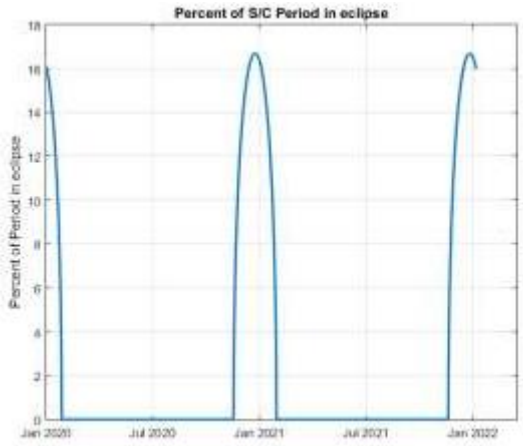

Figure 6. Percentage of a full orbit spent in eclipse as a function of time and for a two-year mission starting January 1, 2020.

4.2. Thermal Considerations

A preliminary thermal analysis was conducted to quantify the temperatures of the elements onboard the CubeSat, especially to check whether the temperature of the detector and the solar panels fall in their operational windows. Figure 6 shows that the CubeSat will spend very long periods exposed to the Sun. Therefore, a worst case hot stationary scenario was analyzed, where the solar panels are exposed to sunlight and where other sides of the CubeSat are exposed to the Earth's thermal radiation and albedo. It was also assumed that the payload was working, because this makes the detector electronics dissipate some heat and warms it up.

Since the detector is a CCD, its dark noise increases as it gets hotter and therefore, the colder it is, the better. Heat from the detector will be evacuated via a dedicated radiator made of copper that is mechanically connected to the detector assembly (Figure 7). This radiator is thermally decoupled from the rest of the CubeSat and faces deep space to radiate heat to its environment. The mechanical connection between the radiator and the detector, as well as the radiator surface itself, have been optimized to achieve a sufficiently low temperature of the detector allowing observing stars, even in the worst case.

The geometrical and thermal mathematical models (GMM and TMM) of the CubeSat, the payload, and the sub-units are built in ESATAN software. The main

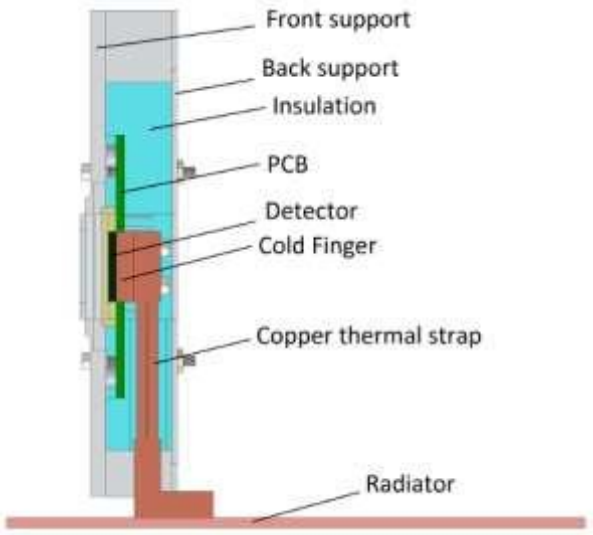

Figure 7. Cross-sectional side-view of the detector assembly and its radiator. The radiator is connected to the back of the detector thanks to a copper cold finger and a copper thermal strap. The blue part surrounding the detector and the copper parts is composed of Permaglas, to minimize the conductive heat transfers between the detector and its mechanical support connected to the satellite structure.

purposes of the GMM are the computation of the radiative exchange factors of each surface and the definition of interfaces and their associated conductance. The TMM defines the thermal and thermo-optical properties of the materials and surfaces. Special attention has been paid to external surfaces that receive heat from the main sources (Sun and Earth) and radiate heat to the cold space. Their surfaces are covered by white paint, to reduce absorbed flux from external sources and increase the power radiated to cold space.

The worst case hot thermal analysis provides the following results for the temperatures of the solar panels (SP) and of the detector, respectively: $T_{SP} \approx 60°C$ and $T_{CCD} \approx 0°C$ 0°C. According to Clyde Space (2017), the solar panels are working up to temperatures of 125°C. The current analysis thus confirms that the panels' temperature is in their operational range. Concerning the detector, T_{CCD} is close to 0°C, where the detector has a level of dark noise approximately equal to 25 e^-/pixel s (e2v Technologies, 2017) – i.e., 500 times higher than the level at −40°C (Table 3). This value of dark signal is quite high, compared to more classical configurations where the sensor is cooled down, but the signal-to-noise ratio calculation in Section 5 demonstrates that it remains acceptable for the current application.

4.3. Power Budget

Several COTS have been considered to quantify the current general characteristics of main CubeSat units, and are described here to reference their power consumption:

- For the onboard computer (OBC), it is proposed to use an ISIS On Board Computer (ISIS Space, 2017). This space-qualified processing unit has a flight heritage since 2014. Its power consumption amount to 400mW on average, with a peak at 550mW.
- The communication system proposed is composed of the NanoMind A3200 and the NanoCom AX100 (GOMSpace, 2017). The first is an additional OBC that could add some data storage volume and redundancy for the subunits in charge of the control software and the second is a software configurable narrow-band transceiver for ultra-high frequency (UHF) and very high frequency (VHF) transmission that is able to reach the data rate transfer presented in section 3.3. The total peak power consumption is 4W.
- The deployable antenna is the NanoCom ANT430 (GOMSpace, 2017) and is a quasi-omnidirectional canted turnstile antenna. A high power consumption of 10W is associated to this component.
- The ADCS is the FleXcore (Blue Canyon Technologies, 2017) which is a fully integrated ADCS composed of micro reaction-wheels, two star trackers, and a micro-controller. Its maximum power consumption peaks to approximately 4W. Regarding the pointing accuracy of the FleXcore, it is able to achieve ±21.6 arcsec (3σ) for three axes, with a fine attitude determination of the order of 1 arcsec. The accuracy of ±21.6 arcsec is worse than the instrument resolution leading to some uncertainty on the actual positioning of the target on the focal plane. However, the fine determination of the

pointing of the order of the arcsec (Hegel, 2016) will reduce the uncertainty, allowing derivation of the target photometry. Moreover, achieving the best accuracy on the photometry will probably require implementation of a chopping mode similar to that used for the BRITE satellites. Indeed, chopping coupled with an appropriate data processing significantly improved the data quality and specifically the robustness against CCD radiation damage defects for the BRITE satellites (Pablo et al., 2016; Popowicz et al., 2017).

- The solar panels are deployable panels from Clyde Space (2017). Their power generation at 60°C (the temperature derived from the thermal analysis) and at beginning of life (BOL) amounts to 6.91W per panel. At end of life (EOL), a loss of a few percent in the panel efficiency is expected and the final power generation is estimated at 6.01W per panel. The EOL total power generation is then evaluated to 24.04W with a deployable four-panel configuration and 30.05W if a fifth body-mounted panel is added.
- The NanoPower P31U (GOMSpace, 2017), which can store power up to 20Whr and manage an amount of 30W coming from the solar panels, is chosen as a battery and power supply. Its power consumption for the supply management peaks to 0.2W.

Table 5 presents the power budget, summarizing all the units of the CubeSat. The maximal power consumption of each unit is considered and 20% margins are applied for uncertainties. Within those margins, a total power of 30.9W is obtained considering the specific worst case where all the units are working simultaneously at their peak power. This budget complies with the power supply system because, with the fifth solar panel added, 30.05W are generated at EOL at normal Sun incidence. On the other hand, the battery is able to store 20Whr which is sufficient for the eclipses which last 17 min at maximum. However, this consumption of 30.9W is very pessimistic, since this situation will probably not occur. This is why Table 6 considers several more realistic operational phases. It can be concluded from these cases that there is benefit from some margins with respect to the power budget during the mission, even at EOL where the solar panels are less efficient. Indeed, in the most energy-demanding case, "observation + data transfer," a little more than 80% of the available power is engaged. This flexibility on the power consumption can also be used to enhance the sky visibility by relaxing the request of a normal Sun incidence on the solar arrays, thereby allowing tolerance of incidence angles up to 30° from normal.

Table 5. Power Budget

Component	Maximum power consumption (W)	Maximum power consumption with 20% margin (W)
Detector assembly	2.00	2.40
On-board computer	0.55	0.66
Communication system	4.00	4.80
Deployable antenna	10.00	12.00
ADCS	4.00	4.80
Solar panels (mechanism)	5.00	6.00
Battery	0.20	0.24
TOTAL	25.75	30.90

5. Photometric Budget

5.1. Modeling

The aim of the photometric budget is to quantify the amount of photons reaching our detector for any given target star. It will inform about the observing time needed to achieve the requirements (especially the signal to noise ratio (SNR)). Stars are differentiated according to their magnitude V and their effective temperature T_{eff}. Appendix A provides the detailed calculation of the photon flux dN emitted by a star for a small range of wavelength $d\lambda$, the final result being:

$$dN = \frac{8.402 * 10^{34} 10^{-0.4(V - A_V + BC + A_\lambda)} d\lambda}{T_{eff}^4 \lambda^4 \left(\exp\left(\frac{1.439\ 10^8}{\lambda T_{eff}} \right) - 1 \right)}. \quad (1)$$

All the parameters of dN are known for stars of the main sequence except for the color excess E_{B-V} that are encountered in the expression of the interstellar extinction A_V and A_λ. The latter is specific to each source, and

Table 6. Expected Operational Phases During the Mission

Phase	Detector assembly	OBC	Communication system	Antenna	ADCS	Solar panels mechanism	Battery	Total power (20% margin)
Deployment	NO	YES	NO	NO	YES	YES	YES	11.7W
Observation	YES	YES	NO	NO	YES	NO	YES	8.1W
Data transfer	NO	YES	YES	YES	YES	NO	YES	22.5W
Observation + data transfer	YES	YES	YES	YES	YES	NO	YES	24.9W

depends on the environment between the star and the observer. Since it is intended to establish a general photometric budget that is a function of V and T_{eff}, the study considered some extreme values for the stars of interest.

The primary interest focuses on massive stars of spectral type OB down to fifth magnitude. Such stars are the brightest in the UV domain and their influence on their direct neighborhood and on the galactic scale is very important making them very interesting targets to observe (Puls et al., 2008). It was thus expected that most of the targets would be nearby objects with a relatively modest interstellar reddening. Using the Yale Bright Star Catalog, the distribution of A_V was investigated as a function of spectral type and magnitude for over 250 stars, including all bright O-type stars and B-type stars down to spectral type B5. It was found that A_V falls in the range between 0 and 2.5 for all the stars in this sample, with a mean at 0.3. Therefore, it was possible to define two extreme cases for the photometric budget: the first one being the worst case, corresponding to the highest extinction for which $A_V = 2.5$ was adopted, and the second being more realistic, where the absorption is at the sample mean of $A_V = 0.3$. Fixing the value of A_V then sets the values of E_{B-V} and also A_λ (see Appendix A). Knowing all the parameters of the photon flux, it was calculated by integrating dN over the spectral domain – i.e., between 2500 and 3500 Å: $N = \int_{\lambda_1=2500\,\text{Å}}^{\lambda_2=3500\,\text{Å}} dN$. Figure 8 presents the curves of N for several magnitudes V and as a function of T_{eff}.

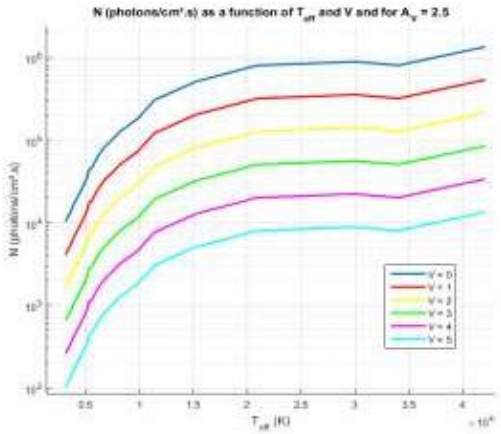

Figure 8. N (expressed in photons/cm².s) as a function of T_{eff} (in K) and V in the highest absorption case ($A_V = 2.5$).

5.2. Signal to Noise Ratio

The required photometric accuracy (Table 1) can be translated into an SNR. It is necessary to reach an accuracy of 0.001 mag, which corresponds to a SNR of 1086. As a first step, the signal is computed as $S = N * T_{exp} * A_{eff} * \eta$ where T_{exp} is the exposure time, A_{eff} is the effective area of the telescope and η is the overall efficiency of the instrument. The η parameter accounts for the reflectivity of the mirrors (between 82% and 92% with an average of 87%) (Melles Griot, 2016), the transmission of the UV filter (50%, per Schott, 2016), and the quantum efficiency of the detector, which is assumed constant over the spectral domain. Considering 10% margins and the lowest efficiencies for all the elements of the telescope, the study found a minimal efficiency of $\eta_{min} = 12\%$, which is used in this Section. Concerning the noise, the photon noise, the dark signal of the detector, the readout noise, and the sky background presented in the stray light section were considered. The expression of the SNR is therefore:

$$SNR = \frac{S}{\sigma_{CCD}} = \frac{N\,A_{eff} t_{exp} \eta}{\sqrt{N\,A_{eff} t_{exp} \eta + n D t_{exp} + n R^2 + 0.007 * N_{SL} A_{eff} t_{exp} \eta}}. \quad (2)$$

In this equation, D is the dark signal, R is the RMS value of the readout noise and n represents the number of pixels illuminated by the PSF (i.e., $n = 4$). The worst case for the SNR computation corresponds to one of

the cooler stars with V = 5 and suffering from the highest extinction, i.e., A_V = 2.5. Figure 9 presents the results of this worst case on the left: to fulfill the requirement for V = 3, the integration time must be approximately equal to 70 seconds. For the other magnitudes V = 4 and 5, it is not possible to achieve the required SNR in the specified integration time of 5 min because of the noise contributed by the stray light. These results are showing the limits of such a small telescope for the observation of the faintest stars among our possible targets. Nevertheless, the right side of Figure 9 corresponds to the same results but for a mean extinction, and in this more realistic case, the requirements of Table 1 are met: an SNR of 1086 is achieved in 105 seconds for a fifth magnitude B5 star, showing that the scientific requirements, and even the goals of Table 1, will be honored for the vast majority of the targets.

Some other effects can affect the SNR of the instrument, such as the aging of the CCD sensor, which is vulnerable to radiation-induced performance changes. The changes are categorized into two types (Burt et al., 2009): changes due to the ionizing dose of energetic charged particles and displacement damage arising from heavy particles (protons and neutrons). The main drawbacks due to these radiations are an increase of the dark signal and a decrease of the charge transfer efficiency. These effects need to be evaluated during pre-flight tests by performing accelerated aging experiment and by calibrating the sensor in-flight. Furthermore, their effect can be mitigated by implementing a chopping mode similar to what is done for the BRITE satellites (Pablo et al., 2016; Popowicz et al., 2017). Another effect is the jitter noise introduced by the reaction wheels of the ADCS. The wheels imbalance induces micro-vibrations that could disturb the spacecraft and make it lose its pointing position, hence moving the target in the focal plane. Knowing the wheels imbalance of the FleXcore allowed computation of the amplitude of the jitter peak, assuming that the satellite is a rigid body, which is equal to 1.15 arcsec. The dynamical behavior of the satellite should be taken into account to refine the jitter peak determination. However, the study considered large safety margins in the assessment of jitter noise, and it can be concluded with confidence that the 1.15 arcsec peak is a realistic value that moves the image of the target within the illuminated pixels, hence not disturbing the signal to noise ratio in a significant way.

5.3. Saturation Issues

The photometric budget has shown benefit from a high quantity of photons at the entrance of the telescope in many cases. Therefore, even for the worst case presented in the previous section, it will not be necessary, and actually not possible, to integrate over five minutes on the same star, because of the limit of the full well capacity C of the detector. The saturation limit can be expressed as:

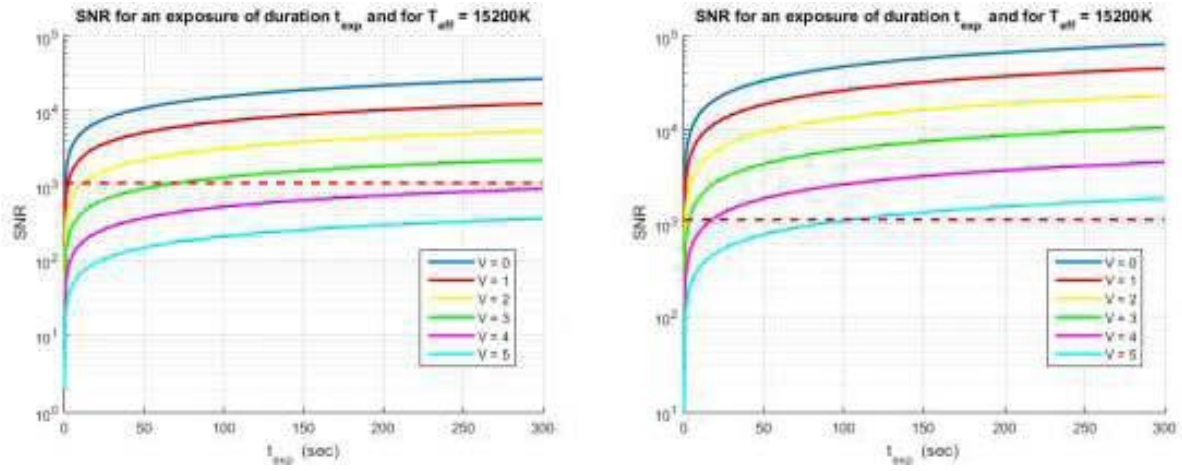

Figure 9. SNR for a star with A_V = 2.5 (left) and A_V = 0.3 (right), T_{eff} = 15 200K and a single exposure of duration t_{exp} . The horizontal red dashed line corresponds to the requirement.

$$\frac{N\,A_{eff}\,\eta\,t_{exp}}{n} + D\,t_{exp} + R^2 + \frac{0.007 * N_{SL}\,A_{eff}\,\eta\,t_{exp}}{n} \leq C. \quad (3)$$

It was assumed that all the energy of the PSF is uniformly spread over the pixels illuminated by the star. This assumption is checked when looking at the spots of Figure 2 for low off-axis angles.

Two extreme cases were considered to demonstrate the feasibility of the observations with our designed telescope. The first case is the worst in terms of saturation where the photon flux is the highest. Consider a putative hot star with an effective temperature of 42 000K, a magnitude V = 0 and A_V = 0. Such an object does not exist in reality, but it allows us to probe the limitations of the instrument. Moreover, consider a situation where the efficiencies of all the optical elements are maximum yielding: η_{max} = 21%. Figure 10 (left) presents the number of generated e^- on a pixel illuminated by the hypothetic hot star as a function of the exposure time. The saturation occurs very quickly (< 0.012s). For this observation case, a more complex strategy must be considered, consisting of several very short exposures that will be combined at the end to recreate the signal. Two exposures of 0.01s are sufficient to reach and even exceed the SNR requirement.

The second case is the worst one for the SNR calculations that was presented in the previous text (i.e., T_{eff} = 15 200 K, V = 3, A_V = 2.5, $\eta = \eta_{min}$). Figure 10 (right) presents the results for this case: saturation now occurs for integration times around 0.18 seconds. It has been shown in Figure 9 (left) that an exposure time of approximately 70 seconds is required to achieve the required SNR. Therefore, it is necessary to combine a number of exposures, to have some margins on the full well capacity. In this case, 472 exposures of 0.1s duration are needed to reach the requirement. Note that to limit the volume of data in the on-board memory, the images related to the same observation have to be processed by the OBC using dedicated software. These numerous observations are still compliant with the maximum observation time of 5 min per target. Imagining that the readout of each exposure also takes 0.1s, the total observation time would be 94.4s, still within the allowed limits. However, the readout of the images will be done much faster considering the possible readout frequency of the detector up to 5 MHz (Table 3).

6. Conclusion

This paper demonstrates that the proposed UV photometer fulfills the scientific requirements. The design is optimized and accommodated to the 3U structure to obtain a fully functional model. The optical layout of the photometer is analyzed regarding optical parameters. The optimization is driven by the volume

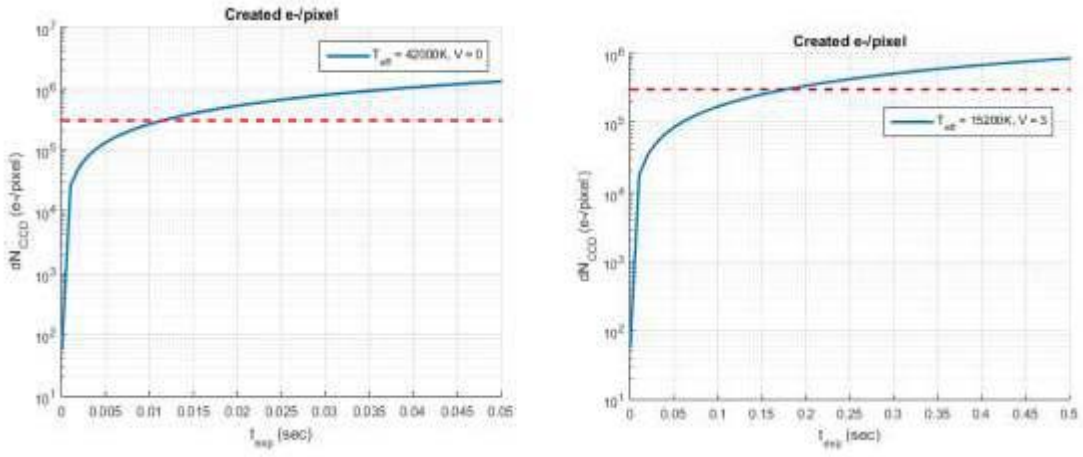

Figure 10. Number of generated on a pixel illuminated by a very hot star considering a low interstellar extinction (left) and a cooler star considering a high interstellar extinction (right). The horizontal red dashed line corresponds to the full well capacity of the detector.

limitations that the CubeSat platform imposes. Moreover, to increase the performance of the imager, a baffling system has been designed and a stray light analysis was performed to quantify the effect of the system.

The system integration led to the 3D model of the spacecraft configuration with its solar panels and subunits. The characteristics of an UV optimized and suitable detector are presented, as well as a discussion on the data storage and transfer relative to the observations made with it. It emerges from this discussion that transfer rates are very constraining, implying that a detector windowing strategy will have to be implemented.

A brief mission analysis was conducted, composed of an orbit definition and a preliminary thermal analysis based on the environment that derives from the orbit. This led to a power budget, associated to the performances of the solar panels for power generation, which proves that the power consumption is not a critical point for the mission considering current COTS.

The photometric budget allowed verification that the optimized design is able to observe the stars of interest, most of the time. Due to noise, mostly induced by the stray light component, it is not possible to observe the fainter stars in the most pessimistic observation configuration. However, it was demonstrated that in more realistic situations, the requirements for all the selected targets are met. A perspective for achieving a better photometric budget would be to design a deployable baffle in front of the current telescope aperture to block the light coming from high off-axis angles. However, such an improvement has significant technical and budgetary impacts.

Acknowledgments

This research was funded through an ARC grant for Concerted Research Actions, financed by the French Community of Belgium (Wallonia-Brussels Federation). The authors also thank Nicolas Berckmans, who assisted with the thermal model and the related analyses in ESATAN in the framework of his master's thesis, entitled Preliminary Thermal Design of a CubeSat, at the University of Liège.

Appendix A: Photometric Budget

For any given star, the absolute magnitude in the V band is given by $M_V = V - DM - A_V$, where V is the apparent magnitude, $DM = 5 \log d - 5$ is the distance modulus (d being expressed in parsecs), and A_V is the interstellar absorption in the V band. The bolometric magnitude is then given by $M_{bol} = M_V + BC$ where BC is the bolometric correction in the V band. The bolometric luminosity (in erg/s) is given by:

$$L_{bol} = 3.03 * 10^{35} * 10^{-0.4 M_{bol}} = 3.03 * 10^{33} * d^2 * 10^{-0.4(V - A_V + BC)} \quad \text{(A1)}$$

It was assumed that the spectrum of the star can be represented by a black-body, whose emission follows the

$$B_\lambda(T_{eff}) = \frac{2\,h\,c^2}{\lambda^5} \frac{1}{\exp(\frac{hc}{\lambda k T_{eff}}) - 1}. \quad \text{(A2)}$$

The power emitted over a narrow range of wavelengths $d\lambda$ hence becomes $d\epsilon = B_\lambda d\lambda$. The integral of this quantity over the full electromagnetic spectrum is $\frac{\sigma T_{eff}^4}{\pi}$. Applying this to a star of bolometric luminosity L_{bol}, one finds: $dF = \frac{L_{bol}\, B_\lambda\, d\lambda\, \pi}{4\,\pi\, d^2\, \sigma\, T_{eff}^4}$. This formula yields the flux of the star over the narrow wavelength interval as one would see it from a distance d with zero interstellar absorption. The corresponding photon flux is $dN = \frac{dF\,\lambda}{hc}$. Therefore:

$$dN = \frac{2\,c\,L_{bol}\,d\lambda}{4\,d^2 \sigma\, T_{eff}^4\, \lambda^4} \frac{1}{\exp\left(\frac{h\,c}{\lambda\,k\,T_{eff}}\right) - 1}. \quad \text{(A3)}$$

Expressing λ and $d\lambda$ in Å and the photon flux dN in photons cm^{-2} s^{-1}, one obtains:

$$dN = \frac{8.402 * 10^{34}\, 10^{-0.4(V - A_V + BC)} d\lambda}{T_{eff}^4 \lambda^4 \left(\exp\left(\frac{1.439\,10^8}{\lambda T_{eff}}\right) - 1\right)}. \quad \text{(A4)}$$

This number further needs to be corrected for the interstellar absorption at the relevant wavelength:

$$dN = \frac{8.402 * 10^{34}\, 10^{-0.4(V-A_V+A_\lambda)} d\lambda}{T_{eff}^4 \lambda^4 \left(\exp\left(\frac{1.439\, 10^8}{\lambda T_{eff}}\right) - 1\right)}. \quad \text{(A5)}$$

The interstellar extinction in the UV can be approximated as a function of wave-number $\sigma = 10000/\lambda$ by (Teays, 2002):

$$\begin{cases} \frac{A_\lambda}{E_{B-V}} = 1.56 = 1.048\,\sigma + \frac{1.01}{((\sigma - 4.60)^2 + 0.280} \\ \qquad for\ 2.70 \le \sigma \le 3.65 \\ \frac{A_\lambda}{E_{B-V}} = 2.29 = 1.848\,\sigma + \\ \frac{1.01}{((\sigma - 4.60)^2 + 0.280}\ for\ 3.65 \le \sigma \le 7.14\,. \quad (A6) \\ \frac{A_\lambda}{E_{B-V}} = 16.17 = 3.20\,\sigma + 0.2975\,\sigma^2 \\ \qquad for\ 7.14 \le \sigma \le 10, \end{cases}$$

where $E_{B-V} = (B-V) - (B-V)_0$ is the color excess expressed as a function of the observed and the intrinsic color index with $A_V \cong 3.1 E_{B-V}$.

References

Aerts, C., Christensen-Dalsgaard, J., and Kurtz, D. W. (2010): *Asteroseismology*, Springer Science + Business Media.

Blomme, R. et al. (2012): CoRoT Observations of O Stars : Diverse Origins of Variability. *Astronomical J. of the Pacific*, Vol. 465, pp. 13–18.

Blue Canyon Technologies. FleXcore. Available at: http://bluecanyontech.com/flexcore/ (accessed October 24, 2017).

Bogges, A. et al. (1978): The IUE Spacecraft and Instrumentation. *Nature*, Vol. 275, pp. 372–377.

Burt, D. et al. (2009): Improving Radiation Tolerance in e2v CCD Sensors, in *Proc. SPIE* 7439, Astronomical and Space Optical Systems, 743902.

Clyde Space. 3U Double-Deployed Solar Array. Available at: https://www.clyde.space/products/26-3u-doubledeployed-solar-array (accessed March 9, 2017).

Conard, S. J. et al. (2000): Far Ultraviolet Spectroscopic Explorer Optical System: Lessons Learned, in *Proc. SPIE* 4139, Instrumentation for UV/EUV Astronomy and Solar Missions, 10.1117/12.410522.

Davenport, J. R. A. (2016): The Kepler Catalog of Stellar Flares. *The Astrophysical J.*, Vol. 829, pp. 23–34.

e2v Technologies. CCD47-20 NIMO Back Illuminated. Available at: https://www.e2v.com/resources/account/download-datasheet/3713 (accessed October 3, 2017).

Fischer, R., Tadic-Galeb, B., and Yoder, P. (2008): *Optical System Design*, 2nd ed. McGraw-Hill.

Gómez de Castro, A. I. et al. (2014): Building Galaxies, Stars, Planets and the Ingredients for Life Between the Stars: The Science Behind the European Ultraviolet-Visible Observatory. *Astrophysics and Space Sci.*, Vol. 354, pp. 229–246.

GOMSpace. Products. Available at: http://www.gomspace.com/index.php?p=products (accessed January 2, 2017).

Gondhalekar, P., Phillips, A., and Wilson, R. (1980): Observations of the Interstellar Ultraviolet Radiation Field from the S2/68 Sky-survey Telescope. *Astronomy and Astrophysics*, Vol. 85, No. 3, pp. 272–280.

Handler, G. (2013): Asteroseismology, in *Planets, Stars and Stellar Systems Volume 4: Stellar Structure and Evolution*, T. Oswalt and M. Barstow (eds.), pp. 207–241.

Harvey, J. and Shack, R. (1975): Light-scattering Characteristics of Optical Surfaces, Optical Sciences Center, University of Arizona, Tucson, Arizona.

Hegel, D. (2016): FlexCore: Low-Cost Attitude Determination and Control Enabling High-Performance Small Spacecraft, in *Proc. of the AIAA/USU Conf. on Small Satellites*, Technical Sessions X: Advanced Technologies II, SSC16-X-7.

ISIS Space. Products. Available at: https://www.isispace.nl/products/ (accessed March 9, 2017).

Leinert, Ch. et al. (1998): The 1997 Reference of Diffuse Night Sky Brightness. *Astronomy and Astrophysics Supp.*, Vol. 127, pp. 1–99.

Mason, K. O. et al. (2001): The XMM-Newton Optical/UV Monitor Telescope. *Astronomy and Astrophysics*, Vol. 365, pp. L36–L44.

Melles Griot. Optical Coatings. Available at: http://mellesgriot.com/ (accessed December 30, 2016).

NSF-NASA (2013): CubeSat-Based Science Missions for Geospace and Atmospheric Research. *National Science Foundation (NSF) Ann. Rep.*

Pablo, H. et al. (2016): The BRITE Constellation Nanosatellite Mission: Testing, Commissioning and Operations. *Pub. of the Astronomical Soc. of the Pacific*, Vol. 128, pp. 125,001.

Persky, M. (1999): Review of Black Surfaces for Space-borne Infrared Systems. *Rev. of Scientific Instruments*, Vol. 70, Issue 5.

Popowicz, A. et al. (2017): BRITE Constellation: Data Processing and Photometry. *Astronomy and Astrophysics*, Vol. 605, id. A26.

Puls, J., Vink, J. S., and Najarro, F. (2008): Mass Loss from Hot Massive Stars. *The Astronomy and Astrophysics Rev.*, Vol. 16, pp. 209–325.

Roach, F. (1964): The Light of the Night Sky: Astronomical, Interplanetary and Geophysical. *Space Science Revs.*, Vol. 3, Issue 4, pp. 512–540.

Schott. Schott UG11 transmission data. Available at: http://www.uqgoptics.com/materials_filters_schott_uvTransmitting_UG11.aspx (accessed December 30, 2016).

Smith, M. et al. (2010): ExoplanetSat: Detecting Transiting Exoplanets Using a Low-cost CubeSat Platform, in *Proc. SPIE* 7731, Space Telescopes and Instrumentation 2010: Optical, Infrared, and Millimeter Wave, 773127-14.

Swartwout, M. (2013): The First One Hundred CubeSats: A Statistical Look. *J. of Small Satellites*, Vol. 2, No. 2, pp. 213–233.

Teledyne e2v. CCD Image Sensors for Space and Ground-based Astronomy. Available at: https://www.e2v.com/products/imaging/ccd-image-sensors-for-space-and-ground-based-astronomy/ (accessed March 9, 2017).

Teays, T. (2000): Ultraviolet Astronomy, in *Allen's Astrophysical Quantities*, A. Cox (ed.), pp. 169–182.

Terebizh, V. (2001): Optimal Baffle Design in a Cassegrain Telescope. *Experimental Astronomy*, Vol. 11, Issue 1, pp. 171–191.

Weiss, W. et al. (2014): BRITE-Constellation: Nanosatellites for Precision Photometry of Bright Stars. *Astronomical Soc. of the Pacific*, Vol. 126, pp. 573–585.

Woellert, K. et al. (2011): CubeSats: Cost-effective Science and Technology Platforms for Emerging and Developing Nations. *Advances in Space Research*, Vol. 47, pp. 663–684.